



Cite this: *Catal. Sci. Technol.*, 2020, **10**, 2652

## Kinetic study of the methane dry ( $\text{CO}_2$ ) reforming reaction over the $\text{Ce}_{0.70}\text{La}_{0.20}\text{Ni}_{0.10}\text{O}_{2-\delta}$ catalyst

Lidia Pino, \* Cristina Italiano, Massimo Laganà, Antonio Vita and Vincenzo Recupero

The kinetic behaviour of the  $\text{Ce}_{0.70}\text{La}_{0.20}\text{Ni}_{0.10}\text{O}_{2-\delta}$  catalyst during the methane dry reforming reaction was investigated in a fixed bed reactor in the temperature range of 923–1023 K with the partial pressure of  $\text{CH}_4$  and  $\text{CO}_2$  ranging between 5 and 50 kPa. The experimental data were fitted using the empirical power-law rate equation and Langmuir–Hinshelwood kinetic models proposed in literature for the Ni– $\text{La}_2\text{O}_3$  catalytic system and based on two-step single- and dual-site mechanisms. The obtained fitting results, after statistical and thermodynamic discrimination, showed that the mechanism of the dry reforming reaction over the  $\text{Ce}_{0.70}\text{La}_{0.20}\text{Ni}_{0.10}\text{O}_{2-\delta}$  catalyst could be successfully described by the two-step dual-site mechanism. The activation energies for the  $\text{CH}_4$  consumption from the power law and Langmuir–Hinshelwood models were estimated to be 91.5 and 136.9  $\text{kJ mol}^{-1}$ , respectively. The lower activation energies for the  $\text{CO}_2$  consumption (70.2 and 100.6  $\text{kJ mol}^{-1}$  from both models) suggested that the  $\text{CO}_2$  activation should faster than  $\text{CH}_4$ . The basic nature of the Ce–La–O sites catalyzed the  $\text{CO}_2$  conversion to oxy-carbonate, decreasing the  $\text{CO}_2$  activation energy compared to that of  $\text{CH}_4$ .

Received 30th October 2019,  
Accepted 18th March 2020

DOI: 10.1039/c9cy02192b

rsc.li/catalysis

## 1. Introduction

The “Paris Agreement” signed by 195 countries under the United Nations Framework Convention on Climate Change (UNFCCC) aims to reduce greenhouse gas emissions, limiting the earth to a 2 °C temperature rise.<sup>1</sup> This ambitious perspective involves, as an energetic strategy, the conversion of the current energetic vector from petroleum to an  $\text{H}_2$ -based energetic vector, which is widely considered an efficient and clean energy source.<sup>2,3</sup> Indeed, as an energy carrier, hydrogen allows decarbonisation in many sectors like transport, industries, space heating and storage for intermittent renewable energy.<sup>4</sup> In this context, methane dry reforming ( $\text{CH}_4 + \text{CO}_2 \rightarrow 2\text{H}_2 + 2\text{CO}$ ,  $\Delta H_{298} = 260.5 \text{ kJ mol}^{-1}$ ) can be considered as a dual global warming addressing technology as it consumes and/or mitigates two greenhouse gases ( $\text{CO}_2$  and  $\text{CH}_4$ ), producing synthesis gas ( $\text{CO}$  and  $\text{H}_2$ ) with an  $\text{H}_2/\text{CO}$  molar ratio closer to unity. This is adequate for the production of valuable synthetic liquid fuels and oxygenated chemicals *via* oxo- and Fischer–Tropsch synthesis processes.<sup>5,6</sup>

Natural gas with a high  $\text{CO}_2$  content yet very abundant in nature<sup>7,8</sup> and biogas produced by the anaerobic digestion of biomass<sup>9,10</sup> can represent significant sources of  $\text{CO}_2$  and  $\text{CH}_4$ . Despite these advantages, methane dry reforming is not yet regarded as an industrially mature process. The main

limitation lies in catalyst deactivation occurring as a result of the large amount of carbon deposition due to the high reaction temperature.<sup>11,12</sup>

Generally, two types of supported catalysts have been applied for the dry reforming reaction: noble metal (Pt, Pd, Rh, Ru, Ir, *etc.*)-based and transition metal (Ni, Co, Fe, *etc.*)-based catalysts. Although noble metals have been found to be less sensitive to coke deposition,<sup>13–16</sup> Ni-based catalysts have been largely studied because of its abundance and low cost. However, a propensity for deactivation can be observed that normally takes place due to the sintering, cooking and phase transformation of the active metal during the reaction.<sup>17,18</sup>

Different strategies have been adopted to increase the resistance to coke deposition in Ni-based catalysts:<sup>19</sup> modification by promoters (structural and chemical),<sup>20</sup> selection of suitable supports ( $\text{CeO}_2$ ,  $\text{MgO}$ ,  $\text{La}_2\text{O}_3$ ,  $\text{CeO}_2\text{--ZrO}_2$ ,  $\text{TiO}_2$ ) able to promote coke gasification by  $\text{CO}_2$  activation;<sup>21,22</sup> the investigation of novel Ni-structures such as core–shell, core–tube and mesoporous framework.<sup>23–25</sup> In addition, it has been evidenced that a fine-tuning and intensification of the interactions between Ni and support can induce better anti-coke and anti-sintering performance of the catalysts.<sup>26,27</sup>

The effect of interactions between the active metal and support, as a result of the formation of a solid solution, on the catalysts' performance during dry reforming reaction has been widely evaluated in literature. Excellent activity and stability have been reported by Hu for the  $\text{NiO}\text{--MgO}$  (or  $\text{CoO}\text{--MgO}$ ) solid solution;<sup>28</sup> the carbon deposition is inhibited by

CNR Istituto di Tecnologie Avanzate per l'Energia “Nicola Giordano”, Via S. Lucia 5, 98126 Messina, Italy. E-mail: lidia.pino@itaee.cnr.it



the isolation effect of small nickel particles formed on the catalytic surface coupled with the surface basicity of  $\text{MgO}$ . Sadykov *et al.* showed that a strong interaction of Ni with  $\text{Ce-Zr-O}$  oxide, as a support in the reduced state, induces a high activity and coking stability of the developed catalyst.<sup>29</sup> Jang *et al.* attributed the excellent activity of the  $\text{MgO}$ -promoted Ni/ $\text{Ce}_{0.8}\text{Zr}_{0.2}\text{O}_2$  sample (equilibrium  $\text{CH}_4$  and  $\text{CO}_2$  conversion for 200 h without carbon deposition) to the high strength of the interactions between the components.<sup>30</sup> Makri *et al.* pointed out that the metal oxide interface in the Ni/ $\text{Ce}_{0.8}\text{Pr}_{0.2}\text{O}_2$  catalyst plays an important role in reducing coke formation under dry reforming conditions.<sup>31</sup>

The catalytic Ni/La-Ce-O<sub>x</sub> mixed oxide system has been widely studied by our research group and successfully applied to reforming reactions.<sup>32,33</sup> In particular, the selected  $\text{Ce}_{0.70}\text{La}_{0.20}\text{Ni}_{0.10}\text{O}_{2-\delta}$  catalyst under appropriate pre-treatment (reduction at 1023 K) exhibited promising activity and stability during the dry reforming reaction.<sup>34</sup> The absence of carbon deposition and stable performance ( $\text{CH}_4$ , conversion = 73%;  $\text{CO}_2$ , conversion = 83%) for 50 h on stream at a gas hourly space velocity (GHSV) of 26 400  $\text{h}^{-1}$ , were observed. In addition, a negligible amount (0.12–0.20%) was deposited at increasing GHSV (52 800–105 600  $\text{h}^{-1}$ ) after  $\text{H}_2$  pre-reduction of the catalyst at 1023 K. From the characterizations of the catalyst, a complex structure has been highlighted that includes: i) a strong metal support interaction (SMSI) evidenced by the suppression of CO and  $\text{H}_2$  chemisorption; ii) the presence of oxygen vacancy defects induced by the partial incorporation of  $\text{Ni}^{2+}$  in the Ce-La-O<sub>x</sub> support with partial exsolution of  $\text{Ni}^{2+}$  and/or  $\text{La}^{3+}$  ions from bulk to surface; iii) the bi-functional role of the support, where  $\text{CeO}_2$  coupled with  $\text{La}_2\text{O}_3$  are involved in  $\text{CO}_2$  adsorption and coke gasification. All of these features seemed to be responsible for the observed catalytic performance.

Kinetics and mechanistic studies over Ni catalysts have been widely reported in literature, as summarized in some recent reviews.<sup>35,36</sup> In the presence of  $\text{La}_2\text{O}_3$  as a support, the proposed mechanisms include the presence of a single- or dual-active site, where the dissociation of methane on Ni particles and carbon gasification by adsorbed  $\text{CO}_2$  on the support sites are the rate-determining steps.<sup>37,38</sup>

In the current study, kinetic measurements over the  $\text{Ce}_{0.70}\text{La}_{0.20}\text{Ni}_{0.10}\text{O}_{2-\delta}$  catalyst were performed. The dependency of the reactant consumption rate and product formation rate on the temperature (923–1023 K) and the reactant partial pressure (5–50 kPa) were evaluated. The results were fitted into a power-law model and the cited Langmuir-Hinshelwood models proposed in literature for the two-step single- and dual-site adsorption mechanisms.

To the best of our knowledge, the intrinsic kinetics of the  $\text{CeO}_2$ - $\text{La}_2\text{O}_3$  mixed oxide-supported Ni catalyst for the dry reforming reaction have not been investigated in detail. The purpose of this study is to combine the characterizations and performance test results from previous investigations with the present kinetics data to propose a plausible kinetics model for the reaction.<sup>34</sup>

## 2. Experimental

### 2.1 Catalyst preparation

The catalyst,  $\text{Ce}_{0.70}\text{La}_{0.20}\text{Ni}_{0.10}\text{O}_{2-\delta}$  (3.66 wt% Ni), was prepared by combustion synthesis as previously reported.<sup>33,34</sup> The metal precursors of cerium ammonium nitrate ( $(\text{NH}_4)_2\text{Ce}(\text{NO}_3)_6 \cdot 6\text{H}_2\text{O}$ ), nickel nitrate ( $\text{Ni}(\text{NO}_3)_2 \cdot 6\text{H}_2\text{O}$ ), and lanthanum nitrate ( $\text{La}(\text{NO}_3)_3 \cdot 6\text{H}_2\text{O}$ ) with oxalyldihydrazide as fuel ( $\text{C}_2\text{H}_6\text{N}_4\text{O}_2$ , all reagents from Aldrich) were dissolved in a minimum amount of  $\text{H}_2\text{O}$ . The mixture was then transferred into an oven furnace heated at 623 K to allow water evaporation, promoting the combustion reaction. A huge amount of fumes were produced and a few seconds after ignition, a fragile foam was formed that easily crumbled into powder. The obtained sample, heated at 873 K in air to burn off the carbonaceous residues, was tableted, ground and sieved to obtain particles with the required size.

### 2.2 Kinetic evaluations

Kinetic studies under different conditions were carried out in a continuous-flow quartz reactor (i.d. = 6 mm) placed in an electric oven. The selection of experimental conditions (reported below) was such that the effect of the external/internal mass and heat transfer could be considered negligible. Weighted amounts of the catalyst (0.011–0.044 g) diluted with quartz of the same size (dilution 1:5) were loaded in the middle part of the reactor and supported on quartz wool. The reaction temperature was measured/controlled by two k-thermocouples. One of the thermocouples was placed inside a thermowell and centered in the catalyst bed; the other was located at the outlet of the catalytic bed. The catalyst activation before the catalytic tests was carried out *in situ* by treatment with a 25%  $\text{H}_2/\text{N}_2$  flow (80 ml  $\text{min}^{-1}$ ) at 1023 K for 2 h, and then the temperature was maintained and/or dropped to the desired reaction temperature. The feed was controlled by mass flow controllers, and the products were analyzed with the help of a gas chromatograph (Agilent 6890 Plus) equipped with FID and TCD detectors. Kinetic measurements were performed in the temperature range of 923–1023 K, employing dilute  $\text{CH}_4:\text{CO}_2:\text{N}_2 = 1:1:3$  feeds. The partial pressure dependencies were evaluated by maintaining the pressure of one reactant at 20 kPa and varying the pressure of the other reactant between 5 to 50 kPa.  $\text{N}_2$ , as the balance gas, was adjusted to maintain the overall pressure constant (101.32 kPa). The gas hourly space velocity was controlled at  $1.2 \times 10^6 \text{ h}^{-1}$  using 0.022 g of the catalyst and appropriate feed flows to obtain significantly lower conversion (<15%) than those defined by thermodynamic equilibrium, and the reaction was controlled by kinetics. For each reactant stream and reaction temperature, the kinetic data were collected after the catalyst was stabilized for about 2 h. The reaction rates, based on the reactant consumption and product formation, were calculated by the following equations:

$$r_{\text{CH}_4, \text{CO}_2} (\text{mol g}^{-1} \text{ s}^{-1}) = \frac{F_{i,\text{in}} \times \text{Conv.}_i}{1000 \times 22.4 \times 60 \times W_{\text{cat}}} \quad (1)$$

$$r_{\text{H}_2, \text{CO}} (\text{mol g}^{-1} \text{ s}^{-1}) = \frac{F_{i,\text{out}}}{1000 \times 22.4 \times 60 \times W_{\text{cat}}} \quad (2)$$

where  $F_{i,\text{in}}$  ( $\text{mol min}^{-1}$ ) is the volume flow rate of the reagent gas,  $F_{i,\text{out}}$  ( $\text{mol min}^{-1}$ ) is the volume flow rate of the component  $i$  in the outflow gas,  $\text{Conv.}_i$  is the reagent conversion and  $W_{\text{cat}}$  (g) is the weight of the catalyst.<sup>39</sup>

### 2.3 Diagnostic tests for mass and heat transfer limitations

In order to evaluate the appropriate experimental conditions under which the effect of the external and internal mass transfer limitations on the methane dry reforming reaction can be considered negligible, preliminary reforming tests were performed by changing the total flow rate and catalyst particle size. The inter-particle limitation tests were performed at a GHSV of  $1.2 \times 10^6 \text{ h}^{-1}$  (reaction conditions: feed composition 20/20/60 vol%; reaction temperature = 923–1023 K, pressure = 101.32 kPa), and showed an invariant rate for flow rates above 200  $\text{ml min}^{-1}$ . This indicated that no external limitations existed under those conditions, as shown in Fig. 1a.

At a selected flow rate of 200  $\text{ml min}^{-1}$ , the absence of the intra-particle limitations was verified by using different average sizes of the catalyst particles (0.180–0.444 mm). As evidenced in Fig. 1b, the reaction rate results were almost

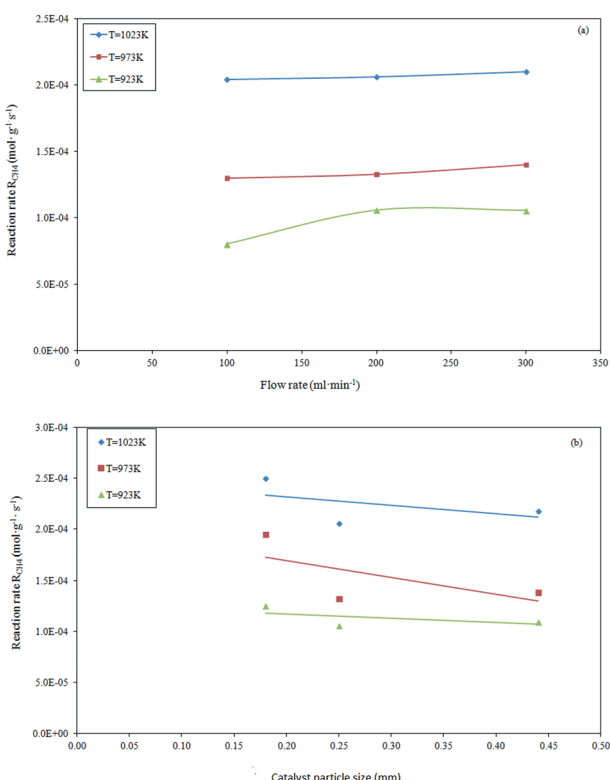


Fig. 1 Effect of volumetric feed flow rate (a) and catalyst particle size (b) on the methane consumption during dry reforming at constant  $\text{GHSV} = 1.2 \times 10^6 \text{ h}^{-1}$ .

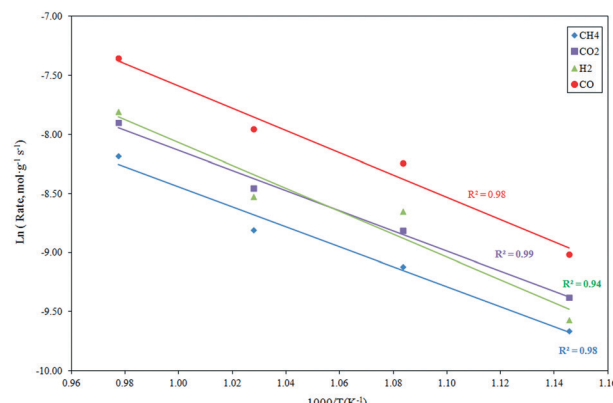


Fig. 2 Influence of the reaction temperature on the  $\text{CH}_4$  and  $\text{CO}_2$  consumption rate, as well as the  $\text{H}_2$  and  $\text{CO}$  formation rate derived at  $101.32 \text{ kPa}$ ,  $\text{CH}_4 : \text{CO}_2 : \text{N}_2 = 1 : 1 : 3$  and  $\text{GHSV} = 1.2 \times 10^6 \text{ h}^{-1}$ .

invariant with particle sizes ranging between 0.254 to 0.444 mm. This suggests that the internal mass transfer limitations can be considered negligible. In summary, the mass transfer limitations and diffusion rate-controlling regime were fully excluded for the conditions selected to perform the catalytic tests, *i.e.*, a flow rate of 200  $\text{ml min}^{-1}$  and average particle size of 0.254 mm.

To further investigate the heat and mass transfer limitations for the reaction over the studied catalyst, suitable diagnostic criteria have been also applied. The effect of intra-/interphase heat transfer limitations on the intrinsic kinetics of the reaction was ruled out using the Mears and Anderson criteria, respectively, represented by the following notations:<sup>40,41</sup>

$$\frac{\Delta H \cdot d_p \cdot \text{rate}_{\text{exp}} \cdot E_a}{h \cdot R \cdot T^2} < 0.3 \quad (3)$$

$$\frac{\Delta H \cdot d_p^2 \cdot \text{rate}_{\text{exp}} \cdot E_a}{\lambda_{\text{eff}} \cdot R \cdot T^2} < 0.3 \quad (4)$$

where  $\Delta H$  is the reaction enthalpy ( $260 \text{ kJ mol}^{-1}$ ),  $\text{rate}_{\text{exp}}$  is the highest reaction rate ( $R_{\text{CO}_2} = 2.07 \times 10^{-4} \text{ mol g}^{-1} \text{ s}^{-1}$ ),  $d_p$  is the catalyst particle diameter ( $254 \times 10^{-6} \text{ m}$ ),  $E_a$  is the experimentally derived activation energy ( $70.17 \text{ kJ mol}^{-1}$ ),  $h$  is the heat transfer coefficient between the gas phase and the catalyst surface ( $908 \text{ W m}^{-2} \text{ K}$ ),  $\lambda_{\text{eff}}$  is the catalyst thermal conductivity ( $11.71 \text{ W m K}$ ),  $R$  is the universal gas constant and  $T$  is the reaction temperature (1023 K). The derived values of  $2.4 \times 10^{-2}$  and  $4.6 \times 10^{-4}$  suggest that the diagnostic criteria are satisfied; thus, the heat transfer effect was not significant. In addition, the effects of the external mass transfer and intra-phase diffusion were checked by application of the Mears and Weisz–Prater criteria, respectively, that can be defined as follows:<sup>42</sup>

$$\frac{\text{rate}_{\text{exp}} \cdot \rho_s \cdot r_p^2 \cdot R \cdot T}{p_{\text{CO}_2} \cdot D_e} < 1 \quad (5)$$

$$\frac{\text{rate}_{\text{exp}} \cdot \rho_s \cdot d_p \cdot R \cdot T \cdot n}{k_c \cdot p_{\text{CO}_2}} \leq 0.3 \quad (6)$$



Table 1 Comparison of apparent activation energy ( $E_a$ ,  $\text{kJ mol}^{-1}$ ) over Ni-based catalysts

Catalyst	Temperature (K)	Reagent compositions (kPa)			$E_a$ ( $\text{CH}_4$ )	$E_a$ ( $\text{CO}_2$ )	$E_a$ (CO)	$E_a$ ( $\text{H}_2$ )	Ref.
		$\text{CH}_4$	$\text{CO}_2$	$\text{N}_2$					
$\text{Ce}_{0.70}\text{La}_{0.20}\text{Ni}_{0.10}\text{O}_{2-\delta}$	873–1023	20	20	60	70.5	71.0	78.3	80.4	This work
$\text{Ni/La}_2\text{O}_3$	773–973	—	—	—	68.0	77.0	—	—	38
$\text{Ni}^\circ$ from 20 LaNi-SBA(10)	813–893	50	50	—	64.7	57.8	63.7	82.7	47
$\text{Ni/CaO-Al}_2\text{O}_3$	893–963	50	50	—	106.7	98.8	103.0	147.4	44
$\text{Ni}_{15}\text{CeMgAl}$	773–873	20	20	60	65.5	62.2	40.8	61.3	39
13.5Ni–2K/10CeO <sub>2</sub> –Al <sub>2</sub> O <sub>3</sub>	873–1073	20	20	60	46.1	46.2	47.4	54.0	45
1Ce <sub>5</sub> Ni <sub>3</sub> Mg/Al	613–673	25	25	50	21.7	23.9	—	—	48
Ni–Co/Al–Mg–O	923–1023	62	62	186	69.4	25.9	61.8	85.1	46
$\text{Ni}/\gamma\text{Al}_2\text{O}_3$	773–973	25	25	50	50.9	56.1	80.5	—	43

where  $\rho_s$  is the catalyst particle density (assumed spherical,  $2500 \text{ kg m}^{-3}$ ),  $n$  is the reaction order (0.31),  $p_{\text{CO}_2}$  is the partial pressure of  $\text{CO}_2$  at the external surface (20 kPa),  $k_c$  is the mass transfer coefficient ( $0.206 \text{ m s}^{-1}$ ). Also, in this case, the derived values of 0.18 and  $8.4 \times 10^{-2}$ , respectively, confirm a negligible influence of the mass transfer on the reaction rate.

## 3. Results

### 3.1 Kinetic evaluations

**Apparent activation energy.** The effect of the temperature on the reaction rate was investigated in the temperature

range 873–1023 K, employing a feed mixture consisting of  $\text{CH}_4:\text{CO}_2:\text{N}_2 = 20:20:60$  vol% under a pressure of 101.32 kPa. The results, in the form of an Arrhenius plot, are depicted in Fig. 2. The apparent activation energies estimated for the  $\text{CH}_4$  and  $\text{CO}_2$  consumption, as well as  $\text{H}_2$  and CO formation, are presented in Table 1 and compared with analogous data from Ni-based catalysts derived from literature. As evident, the apparent activation energy can reach very different values over the different catalytic systems applied to the reaction. The support of the Ni catalysts can significantly influence the activation energy by altering the rate-controlling step in the reaction sequence.<sup>45,49</sup> Bradford and Vannice pointed out that the activation energies for the reforming reaction, carried out with Ni catalysts supported on different supports, were typically included in the range 30–100  $\text{kJ mol}^{-1}$ . Conversely, high values of up to 160  $\text{kJ mol}^{-1}$  have been obtained for some classes of catalysts.<sup>50</sup>

In the current investigation with the  $\text{Ce}_{0.70}\text{La}_{0.20}\text{Ni}_{0.10}\text{O}_{2-\delta}$  catalyst, the activation energies for  $\text{CH}_4$  and  $\text{CO}_2$  consumption were very close and comparable with analogous data reported by Sierra-Gallego *et al.* for the  $\text{Ni/La}_2\text{O}_3$  catalytic system.<sup>38</sup> The apparent activation energies for hydrogen and CO were greater than those for  $\text{CH}_4$  and  $\text{CO}_2$ , suggesting that the rate-determining step for CO and  $\text{H}_2$  formation are different from those for  $\text{CH}_4$  and  $\text{CO}_2$  consumption. In addition, the activation energy for  $\text{H}_2$  production was higher than that for the formation of CO. This could be related to the parallel occurrence of the reverse water gas shift reaction (RWSR) that influences the reaction mechanism.<sup>45</sup>

### Effect of reactant partial pressures on dry reforming rate.

The influence of the partial pressure of  $\text{CH}_4$  and  $\text{CO}_2$  on the reforming rate was evaluated at a pressure of 101.32 kPa in the temperature range of 923–1023 K. The effect of the  $\text{CH}_4$  partial pressure on the consumption rate of  $\text{CH}_4$  was evaluated at a constant  $\text{CO}_2$  partial pressure of 20 kPa as the  $\text{CH}_4$  partial pressure was increased from 5 to 50 kPa. The results evaluated at the different temperatures are depicted in Fig. 3a.

As evident, the rate of methane consumption was noticeably influenced by the  $\text{CH}_4$  partial pressure over the whole experimental range of 5–30 kPa. A further increase of

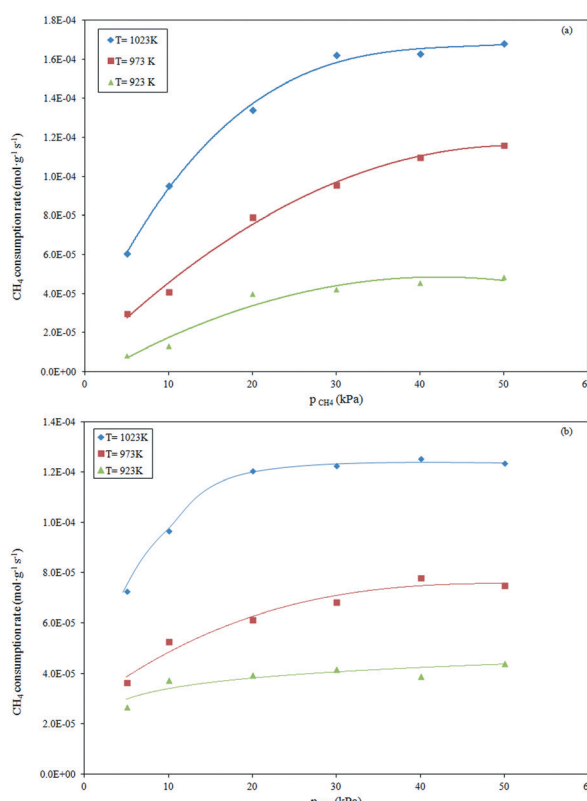


Fig. 3 Effect of variation of partial pressure of  $\text{CH}_4$  (a) and  $\text{CO}_2$  (b) at constant  $p_{\text{CO}_2}$  and  $p_{\text{CH}_4}$ , respectively, on the reaction rate over the  $\text{Ce}_{0.70}\text{La}_{0.20}\text{Ni}_{0.10}\text{O}_{2-\delta}$  catalyst in the temperature range of 923–1023 K.



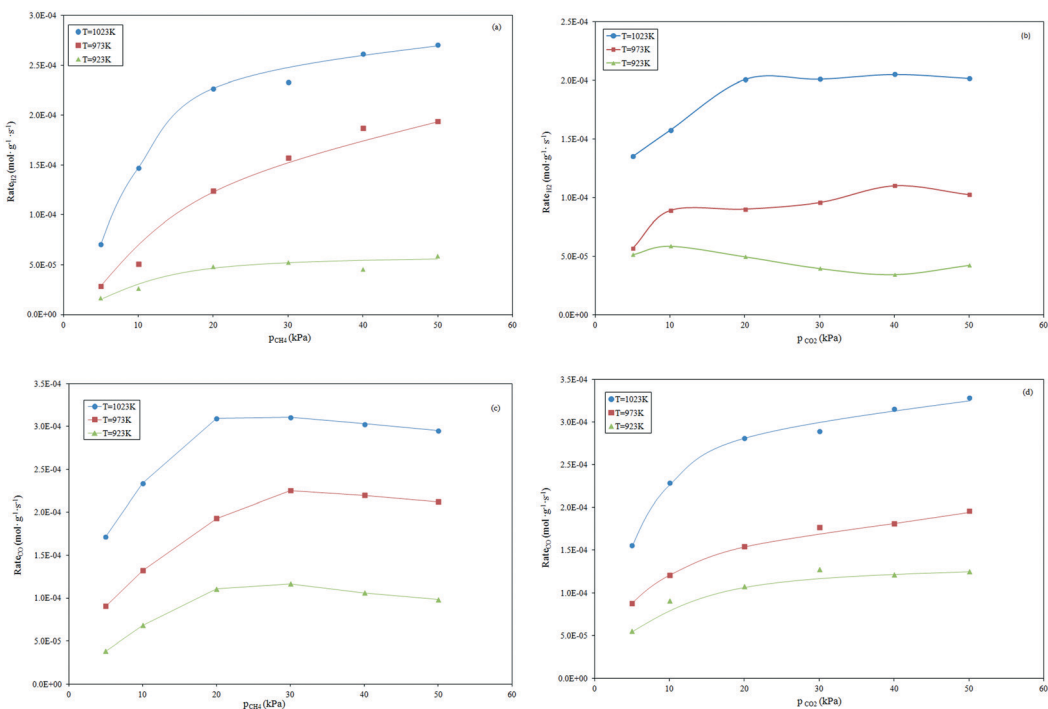


Fig. 4 Effect of the alteration of  $CH_4$  partial pressure (a and c) and  $CO_2$  (b and d) at constant  $p_{CO_2}$  and  $p_{CH_4}$ , respectively, on the  $H_2$  and  $CO$  formation rates.

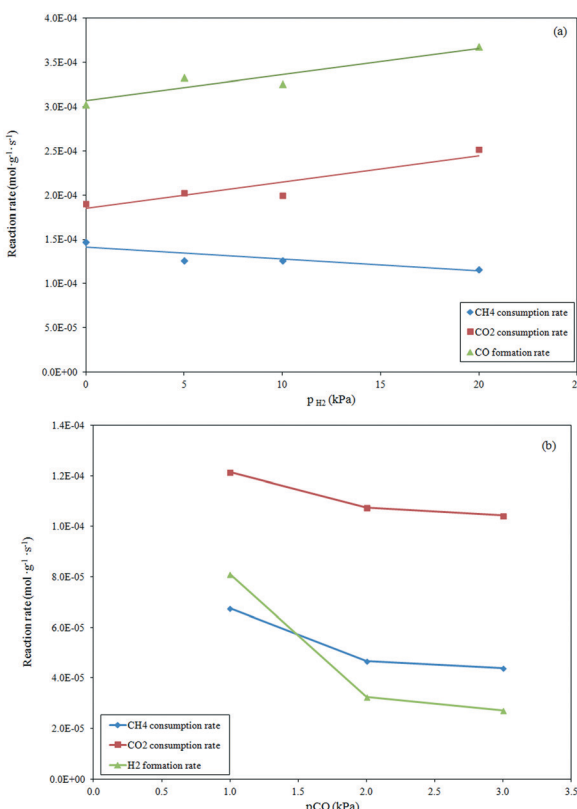


Fig. 5 Influence of  $H_2$  (a) and  $CO_2$  addition (b) to the feed mixture ( $T = 1023$  K,  $p_{CH_4} = p_{CO_2} = 10$  kPa) on the reaction rates.

the  $CH_4$  partial pressure up to 30 kPa induced a less significant effect in the consumption rate. This behavior was observed at high reaction temperatures (973–1023 K). At 923 K, the reforming rate was sensitively affected by the low partial pressures of  $CH_4$  ( $\leq 20$  kPa), remaining almost unchanged with further increase of the  $CH_4$  partial pressure.

The effect of the variation of the  $CO_2$  partial pressure on the rate of the methane consumption is depicted in Fig. 3b. It can be seen that the methane consumption rate increased with increasing  $CO_2$  partial pressure in the range of 5–20 kPa, remaining almost constant at higher partial pressures (20–50 kPa). The relatively constant reaction rate, recorded at all investigated reaction temperatures, can be ascribed to a limitation of the thermodynamic equilibrium of the limiting reactant  $CH_4$  ( $p_{CH_4} = 20$  kPa).

In addition, the effect of the  $CO_2$  partial pressure appeared less significant in the tests carried out at a lower temperature (923 K) in relation to analogous tests at higher temperatures (973–1023 K).

A comparison of Fig. 3a and b suggests that the  $CH_4$  consumption rate was more sensitive to the  $CO_2$  partial pressure than the  $CH_4$  partial pressure at low  $CH_4$  and  $CO_2$  partial pressures, respectively. From these results, a stronger  $CO_2$  adsorption on the catalyst surface can be derived than  $CH_4$  adsorption due to the strong interaction of the  $CO_2$  molecule with the basic surface of the mixed  $Ni-La-CeO_x$  oxides, as previous envisaged.<sup>32</sup> The presence of the  $Ce_2O_3$  support from the pre-reduction step of the catalyst can enhance  $CO_2$  adsorption by forming the strong ionic oxide  $Ce_2O_2CO_3$ . The sequential dissociation of the carbonate

Table 2 Estimation of kinetics parameters from the power law model

Reaction species	Kinetics parameters			$E_a$ (kJ mol <sup>-1</sup> )	$R^2$	Rmsd (mol g <sup>-1</sup> s <sup>-1</sup> )	$\sigma$ (mol g <sup>-1</sup> s <sup>-1</sup> )
	$m$	$n$	$A$ (mol g <sup>-1</sup> s <sup>-1</sup> ) kPa <sup>-(m+n)</sup>				
CH <sub>4</sub>	0.50	0.20	0.66	91.50	0.97	$8.6 \times 10^{-6}$	$4.7 \times 10^{-5}$
CO <sub>2</sub>	0.29	0.31	0.10	70.17	0.97	$9.9 \times 10^{-6}$	$6.0 \times 10^{-5}$
H <sub>2</sub>	0.54	0.15	5.62	105.41	0.95	$1.7 \times 10^{-5}$	$1.0 \times 10^{-4}$
CO	0.26	0.28	0.53	78.52	0.96	$1.8 \times 10^{-5}$	$7.8 \times 10^{-5}$

Rmsd: root mean square deviation;  $\sigma$ : standard deviation.

species into CO<sub>2</sub> and further to CO and O generates oxygen species able to react with carbon deposits at the Ni–Ce<sub>2</sub>O<sub>3</sub> interface.<sup>51</sup> Similarly, CO<sub>2</sub> can adsorb onto La<sub>2</sub>O<sub>3</sub> (present on the surface) to form La–oxycarbonates, which in turn react with the carbon formed from CH<sub>4</sub> activation at the metal–La interface, cleaning the surface of the catalyst from carbon accumulation. This scavenging effect of the carbonate species on carbon from Ni has been proven to be responsible for the stability evidenced by the Ni/La<sub>2</sub>O<sub>3</sub>, Rh/La<sub>2</sub>O<sub>3</sub> and Rh/La<sub>2</sub>O<sub>3</sub>–SiO<sub>2</sub> catalysts.<sup>37,44,52–54</sup> Finally, the presence of oxygen vacancies on CeO<sub>2</sub>–La<sub>2</sub>O<sub>3</sub> in solid solution can promote the dissociation of adsorbed CO<sub>2</sub>, generating lattice oxygen that reacts with the carbon atom. This can play a fundamental role in the stability of the doped Ni–CeO<sub>2</sub> catalytic system.<sup>31</sup> Results of the previous investigation with the Ce<sub>0.70</sub>La<sub>0.20</sub>Ni<sub>0.10</sub>O<sub>2– $\delta$</sub>  catalyst, under analogous experimental conditions after 50 h of reaction, showed the absence of carbon deposition.<sup>34</sup>

**Effect of reactant partial pressures on product formation rates.** The formation rates of H<sub>2</sub> and CO as a function of the partial pressure of the reactants are depicted in Fig. 4. The rate of H<sub>2</sub> formation for constant CO<sub>2</sub> partial pressure increases linearly by increasing the CH<sub>4</sub> partial pressure in the range 5–20 kPa. A more limited increase at higher CH<sub>4</sub> partial pressure was recorded, as shown in Fig. 4a. This suggests that the dry reforming and RWGS reactions rates become lower in the presence of a limited CO<sub>2</sub> amount. This is supported by the experiments conducted at constant CH<sub>4</sub> partial pressure. Depicted in Fig. 4b, the increase in the CO<sub>2</sub>

partial pressure up to the stoichiometric value (20 kPa) involves a noticeable increase in the H<sub>2</sub> formation rates that become invariant at higher partial pressures of CO<sub>2</sub>. The equilibrium that is established between H<sub>2</sub> produced by reforming and consumed by RWGS results responsible of the observed trend. The dependence of the CO formation rate on the partial pressures of CH<sub>4</sub> and CO<sub>2</sub>, is depicted in Fig. 4c and d, respectively.

A quasi-linear dependence of the CO formation rate on the CH<sub>4</sub> partial pressure ranging between 5 to 20 kPa can be observed. Conversely, a light decrease in the CO formation rate at a high partial pressure of CH<sub>4</sub> (Fig. 4c) was observed. This could be due to the effect of side reactions such as RWGS, that limit the CO formation when CO<sub>2</sub> is the limiting reagent. This is supported by the observation of Fig. 4d: the CO formation increases progressively by increasing the partial pressure of CO<sub>2</sub>. The observed trend agrees well with those reported by other authors such as Osazuwa *et al.* with the SmCoO<sub>3</sub> perovskite catalyst,<sup>55</sup> Nandini *et al.* who evaluated the catalytic activity of a Ni–K/CeO<sub>2</sub>–Al<sub>2</sub>O<sub>3</sub> sample,<sup>45</sup> and Fan *et al.* who applied a bimetallic Ni–Co/MgO–ZrO<sub>2</sub> catalyst to the dry reforming reaction.<sup>20</sup>

**Effect of product partial pressures on dry formation rates.** The effect of H<sub>2</sub> in the feed on the dry reforming rate was investigated in the range of 5–20 kPa at a constant CH<sub>4</sub> and CO<sub>2</sub> partial pressure of 10 kPa and reaction temperature of 1023 K. The results depicted in Fig. 5a show that the increase in the H<sub>2</sub> partial pressure induced a light inhibition of the methane consumption rate, while exerting a positive effect on the CO<sub>2</sub> consumption rate and CO production rate. This behavior, attributable to the occurrence of the reverse water gas shift reaction, shows that the Ni–H produced on the surface can reach an equilibrium state with the hydrogen product from the dry reforming reaction.<sup>44</sup>

The effect of the increased CO partial pressure from 1 to 3 kPa in the feed stream on the reaction rates is evidenced in Fig. 5b. The reforming rates were slightly influenced by the CO partial pressure. A decrease in the reforming rate was observed for  $p_{CO}$  (up to 2 kPa) that remained almost constant with further increases in the CO partial pressure. Taking in consideration that the CH<sub>4</sub> dissociation and CO adsorption occurred on the Ni active sites, the inhibition effect of CO on the reaction rate was due to the competitive adsorption of CO on active sites that limited the adsorption/dissociation of CH<sub>4</sub> for which the reforming rate decreased. The invariant

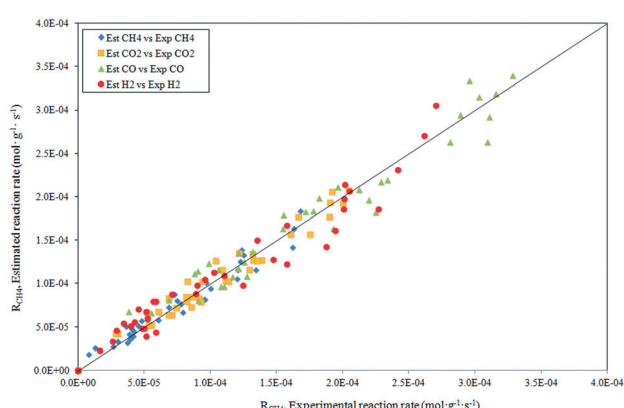


Fig. 6 Statistical fit of the postulated power law model showing the comparison of the rate predicted by the model to the experimental rate.



Table 3 Activation energy from the power law reported in the literature

Catalyst	Temperature (K)	Partial pressure (kPa)	$E_{\text{CH}_4}$ (kJ mol <sup>-1</sup> )	$E_{\text{CO}_2}$ (kJ mol <sup>-1</sup> )	$E_{\text{CO}}$ (kJ mol <sup>-1</sup> )	$E_{\text{H}_2}$ (kJ mol <sup>-1</sup> )	Ref.
10.1Ni/MgO	673–823	5–53	92.10	87.9	87.90	146.51	49
1.22Ni/TiO <sub>2</sub>	673–823	"	108.8	87.9	96.28	133.95	"
Co/La <sub>2</sub> O <sub>3</sub>	923–1023	5–50	96.44	72.22	69.71	101.50	60
Ni/Al <sub>2</sub> O <sub>3</sub>	850–1000	17–51	76.0				59
5Ni/CeO <sub>2</sub> –SiO <sub>2</sub> - <i>c</i>	703–733	20–40	154.7				61
5Ni/CeO <sub>2</sub> –SiO <sub>2</sub> - <i>p</i>	"	"	97.3				"
4.7Ni/ZnO	863–883	4.5–11	110.7	118.4			62
4.8Ni–4.3MgO/ZnO	743–763	"	97.4	106.3			"

Table 4 Langmuir–Hinshelwood kinetic models parameters

Model no.	Temperature (K)	Kinetic constant				Rmsd (mol g <sup>-1</sup> s <sup>-1</sup> )	$\sigma$ (mol g <sup>-1</sup> s <sup>-1</sup> )	
		$K_1$ (kPa <sup>-1</sup> )	$k_2$ (mol g <sup>-1</sup> s <sup>-1</sup> )	$K_3$ (kPa <sup>-1</sup> )	$k_4$ (mol g <sup>-1</sup> s <sup>-1</sup> )			
1	1023	0.0323 (1.8 × 10 <sup>-2</sup> )	0.00036 (1.5 × 10 <sup>-4</sup> )	0.0037 (3.5 × 10 <sup>-1</sup> )	0.00815 (7.0 × 10 <sup>-2</sup> )	0.97	2.3 × 10 <sup>-5</sup>	2.6 × 10 <sup>-3</sup>
	973	0.0250 (1.3 × 10 <sup>-2</sup> )	0.00025 (9.4 × 10 <sup>-5</sup> )	0.0080 (1.0 × 10 <sup>-1</sup> )	0.00267 (3.4 × 10 <sup>-1</sup> )	0.96	3.0 × 10 <sup>-6</sup>	7.5 × 10 <sup>-6</sup>
	923	0.0811 (5.4 × 10 <sup>-2</sup> )	0.00005 (1.8 × 10 <sup>-5</sup> )	0.0100 (3.0 × 10 <sup>-2</sup> )	0.00299 (8.1 × 10 <sup>-3</sup> )	0.91	7.9 × 10 <sup>-6</sup>	1.8 × 10 <sup>-5</sup>
2	1023	0.0285 (2.7 × 10 <sup>-2</sup> )	0.00040 (3.2 × 10 <sup>-5</sup> )	0.0069 (2.5 × 10 <sup>-2</sup> )	0.0043 (1.4 × 10 <sup>-3</sup> )	0.97	1.5 × 10 <sup>-5</sup>	8.7 × 10 <sup>-4</sup>
	973	0.0466 (5.4 × 10 <sup>-2</sup> )	0.00019 (1.8 × 10 <sup>-4</sup> )	0.0100 (9.0 × 10 <sup>-2</sup> )	0.0024 (1.1 × 10 <sup>-3</sup> )	0.93	1.4 × 10 <sup>-5</sup>	2.8 × 10 <sup>-4</sup>
	923	0.0679 (7.7 × 10 <sup>-2</sup> )	0.00007 (5.6 × 10 <sup>-5</sup> )	0.0181 (3.2 × 10 <sup>-1</sup> )	0.0012 (8.2 × 10 <sup>-4</sup> )	0.92	2.4 × 10 <sup>-6</sup>	4.8 × 10 <sup>-6</sup>

Rmsd: root mean square deviation.  $\sigma$ : standard deviation, (values in parenthesis are the standard deviation for the kinetic constants).

Table 5 Models screening using change in entropies and enthalpies for CH<sub>4</sub> and CO<sub>2</sub>

Reagent	Model no.	$\Delta H$ (kJ mol <sup>-1</sup> )	$\Delta S$ (kJ mol <sup>-1</sup> K)	$R^2$	Criteria (eqn (20))
CH <sub>4</sub>	1	-74.04	-102.92	0.58	10 ≤ 102.92 ≤ 115.85 (yes)
	2	-68.84	-97.87	0.98	10 ≤ 97.87 ≤ 108.58 (yes)
CO <sub>2</sub>	1	-77.25	-121.20	0.89	10 ≤ 121.20 ≤ 120.35 (no)
	2	-76.49	-117.21	0.99	10 ≤ 117.21 ≤ 119.30 (yes)

CH<sub>4</sub> consumption rate observed at high CO partial pressure can suggest a limited CO adsorption on the Ni active sites.

### 3.2 Kinetic modeling

**Power law model.** The obtained kinetic data, including the reaction rates and partial pressures of the reactants (CH<sub>4</sub> and

CO<sub>2</sub>), were first fitted into the empirical power law model. This provides a rough estimation of the reaction parameters even though it does not account for the reaction mechanisms. The empirical power law model for the dry reforming reaction is given in the following equation:

$$r_i = A \exp\left(\frac{-E_a}{RT}\right) p_{\text{CH}_4}^m p P_{\text{CO}_2}^n \quad (7)$$

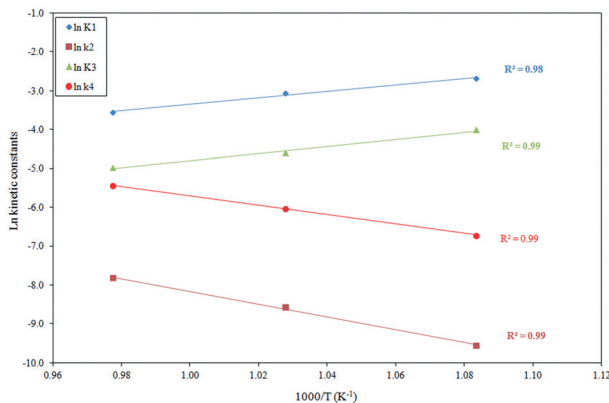


Fig. 7 Effect of the temperature on the adsorption ( $K_1$  and  $K_3$ ) and reaction constants ( $k_2$  and  $k_4$ ) for the Langmuir–Hinshelwood kinetic model (model 2).

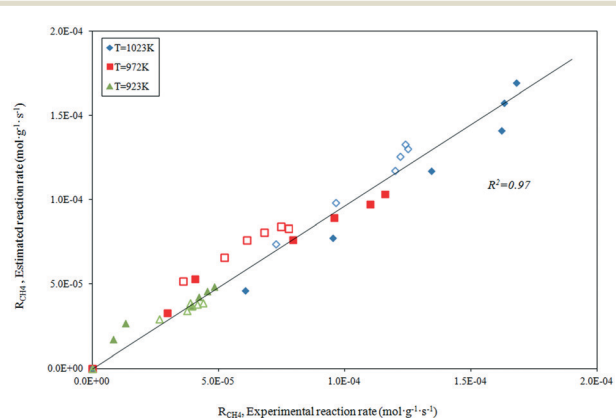


Fig. 8 Statistical fit of the postulated model 2 comparing the rate predicted by the model to the experimental rate.



where  $r_i$  represents the consumption rates of  $\text{CH}_4$  and  $\text{CO}_2$ , as well as the formation rates of  $\text{H}_2$  and  $\text{CO}$ ;  $A$  represents the pre-exponential factor,  $E_a$  is the activation energy;  $R$  is the universal gas constant;  $p_{\text{CH}_4}$  and  $p_{\text{CO}_2}$  are the partial pressures of  $\text{CH}_4$  and  $\text{CO}_2$ , respectively, with  $m$  and  $n$  as the related reaction orders; and  $T$  is the absolute reaction temperature.

The SOLVER function, available in Excel spreadsheets, was employed to evaluate the kinetic parameters from the nonlinear power law model.<sup>56,57</sup> The goodness of fit was determined by the coefficient of determination ( $R^2$ ). The estimated values of the kinetic parameters, as well as the corresponding  $R^2$ , Rmsd (residual sum of square) and  $\sigma$  (standard deviation) values are summarized in Table 2. It can be seen that the reaction rates for the reactants and products were satisfactorily predicted with  $R^2 \geq 0.95$ .

Activation energies of approximately 91.5  $\text{kJ mol}^{-1}$  and 70.17  $\text{kJ mol}^{-1}$  were derived for  $\text{CH}_4$  and  $\text{CO}_2$  consumption, respectively, as evidenced in Table 2. The activation energy of the  $\text{CH}_4$  consumption was higher than that of the  $\text{CO}_2$  consumption. This indicates that the  $\text{CH}_4$  activation is more temperature-sensitive than that of  $\text{CO}_2$ .

The lower  $\text{CO}_2$  activation energy related to the methane activation energy implied furthermore that the rate of  $\text{CO}_2$  consumption was faster than that for  $\text{CH}_4$ . Thus, the  $\text{CO}_2$  conversion was higher than the  $\text{CH}_4$  conversion.<sup>58</sup>

The reaction orders obtained for the  $\text{CH}_4$  consumption ( $m = 0.50$ ;  $n = 0.20$ ) indicate that the  $\text{CH}_4$  partial pressure significantly influences the methane reforming. In addition, the  $\text{CO}_2$  consumption is influenced by the  $\text{CO}_2$  partial pressure ( $m = 0.29$ ;  $n = 0.31$ ).

The activation energies of  $\text{H}_2$  (105.41  $\text{kJ mol}^{-1}$ ) and  $\text{CO}$  (78.52  $\text{kJ mol}^{-1}$ ) are comparable to that of  $\text{CH}_4$  and  $\text{CO}_2$ , respectively. Therefore, it can be derived that the  $\text{H}_2$  formation was predominantly influenced by  $\text{CH}_4$ , while the  $\text{CO}$  formation was primarily influenced by  $\text{CO}_2$ . Furthermore, both values were higher than those for the  $\text{CH}_4$  and  $\text{CO}_2$  consumption. This suggests, as previously observed, that the rate-determining steps for the  $\text{H}_2$  and  $\text{CO}$  formation are different from those for the reagent consumption.

The activation energy for  $\text{H}_2$  production, noticeably higher than that  $\text{CO}$ , is a clear indication of the influence of the RWGS reaction on the  $\text{H}_2$  formation. A comparison of the experimental rates for  $\text{CH}_4$  and  $\text{CO}_2$  consumption, as well as for the  $\text{H}_2$  and  $\text{CO}$  formation with those predicted by the power law model, are given in Fig. 6. A good agreement between the predicted and experimental values emerged.

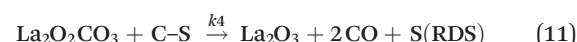
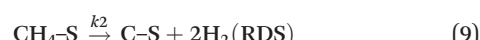
The derived kinetic parameters are very similar to the reported values by Bradford and Vannice<sup>49</sup> and Ayodele *et al.* for the reaction carried out with  $\text{Ni}/\text{MgO}$  and  $\text{Co}/\text{La}_2\text{O}_3$ ,<sup>60</sup> respectively, as evidenced in Table 3. Its results are noticeably higher than the activation energy reported by Takano *et al.* over a traditional  $\text{Ni}/\text{Al}_2\text{O}_3$  (cordierite) catalyst.<sup>59</sup> Although the different supports have different influences on the activity of the metallic phase, this could be ascribed to the high interaction occurring between  $\text{Ni}$  and the  $\text{La}-\text{CeO}_x$  support.

Indeed, Bradford and Vannice pointed out that with the  $\text{Ni}-\text{TiO}_2$  catalyst, the SMSI induced a noticeable value of the activation energy (108  $\text{kJ mol}^{-1}$ ) that increased to 171.6  $\text{kJ mol}^{-1}$  after 18 h of stream.<sup>49</sup> In this case, the migration of  $\text{TiO}_x$  on the  $\text{Ni}$  surface may increase the activation barrier for methane dissociation. Recently, Yan *et al.* showed that the close metal-support interface between  $\text{Ni}$  and  $\text{CeO}_2$  in the  $\text{Ni}-\text{CeO}_2-\text{SiO}_2$  catalyst led to a substantial decrease in the activation energy from 154.7  $\text{kJ mol}^{-1}$  ( $\text{Ni}-\text{CeO}_2-\text{SiO}_2$  sample C) to 97.3  $\text{kJ mol}^{-1}$  with the sample in the absence of interactions ( $\text{Ni}-\text{CeO}_2-\text{SiO}_2$  sample P).<sup>61</sup> Analogous evidence emerged from the study reported by Singha *et al.*, where the methane activation energy of the  $\text{Ni}/\text{ZnO}$  catalyst decreased significantly from 110.7  $\text{kJ mol}^{-1}$  to 97.4  $\text{kJ mol}^{-1}$  by the addition of  $\text{MgO}$  in the catalyst formulation, inducing high  $\text{Ni}$  dispersion and metal-support interactions.<sup>62</sup> Therefore, other models may be more appropriate than the power law. In the following section, the Langmuir–Hinshelwood mechanism models proposed in the literature for the  $\text{Ni}-\text{La}_2\text{O}_3$  catalytic system (and as previously mentioned) were applied to evaluate the kinetic mechanism of the current sample.

**Langmuir–Hinshelwood models.** Many studies related to the kinetics of methane reforming with  $\text{CO}_2$  are generally based on mechanistic steps that include: i) the dissociation/activation of  $\text{CH}_4$  and  $\text{CO}_2$ ; ii) adsorption of elemental and intermediate species on active sites; iii) formation of products *via* surface reactions; iv) desorption of product species.<sup>63</sup> The fundamental study carried out by L. M. Aparicio showed that there is not a single rate-determining step (RDS) in the reaction.<sup>64</sup> Therefore, in most cases, the  $\text{CH}_4$  and  $\text{CO}_2$  dissociation or activation are considered to be the RDS.

Based on DRIFT (diffuse reflectance infrared Fourier transform) and SSITKA (steady-state isotopic transient kinetic analysis) studies, Verykios and co-workers proposed a mechanistic sequence for the  $\text{Ni}/\text{La}_2\text{O}_3$  catalytic system where  $\text{CH}_4$  cracking is a slow step, while the  $\text{CH}_4$  adsorption is at equilibrium.<sup>65–67</sup> The strong interaction occurring between  $\text{CO}_2$  and  $\text{La}_2\text{O}_3$  that leads to the formation of the  $\text{La}_2\text{O}_2\text{CO}_3$  species, can be considered a fast step at equilibrium. Conversely, the reaction between this formed species with  $\text{Ni}$  particles at the  $\text{Ni}/\text{La}_2\text{O}_2\text{CO}_3$  interface oxygenated species becomes a slow step.<sup>37</sup>

This mechanistic step can be synthetically represented by the following reactions:



In addition, the simultaneous occurrence of RGSR includes the sequence of the following reaction steps:

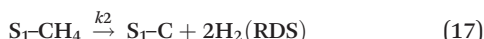
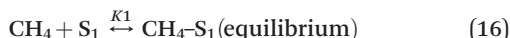


On this basis, the authors derived the following rate expression for the methane consumption:

$$r_{\text{CH}_4} = \frac{K_1 k_2 K_3 k_4 p_{\text{CH}_4} p_{\text{CO}_2}}{K_1 K_3 k_4 p_{\text{CH}_4} p_{\text{CO}_2} + K_1 k_2 p_{\text{CH}_4} + K_3 k_4 p_{\text{CO}_2}} \quad (\text{Model 1})$$

where  $K_1$  is the adsorption equilibrium constant for  $\text{CH}_4$ ;  $k_2$  is the rate constant of methane cracking on the metallic surface;  $K_3$  is the adsorption equilibrium constant of the reaction between  $\text{CO}_2$  and  $\text{La}_2\text{O}_3$ ;  $k_4$  is the rate constant of the reaction between the oxycarbonate species and carbon deposited on the Ni surface.

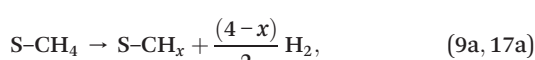
Sierra-Gallego *et al.* studied the kinetic behaviour of the  $\text{Ni}/\text{La}_2\text{O}_3$  catalyst obtained from the reduction of  $\text{LaNiO}_3$  perovskite structure.<sup>38</sup> From XPS (X-ray photoelectron spectroscopy) after the catalytic tests, the authors derived that the Ni particles were partially covered by the  $\text{La}_2\text{O}_2\text{CO}_3$  species due to the migration of  $\text{La}_2\text{O}_3$  over the metal particles. From this evidence, the authors developed a rate reaction equation including, for the first time, the presence of two active sites on the catalyst surface: metallic nickel particles and the  $\text{La}_2\text{O}_3$  metal support. Assuming a negligible  $\text{H}_2$  and  $\text{CO}$  surface coverage, the proposed dual active-site mechanism involves the following steps:



where  $\text{S}_1$  represents the metallic active site ( $\text{Ni}^\circ$ ) and  $\text{S}_2$  is the  $\text{La}_2\text{O}_3$  support as the active site. The related rate model assumes the following form:

$$r_{\text{CH}_4} = \frac{K_1 k_2 K_3 k_4 p_{\text{CH}_4} p_{\text{CO}_2}}{K_3 k_4 p_{\text{CO}_2} + K_1 K_3 k_4 p_{\text{CH}_4} p_{\text{CO}_2} + K_1 k_2 p_{\text{CH}_4} + K_1 k_2 K_3 p_{\text{CO}_2}} \quad (\text{Model 2})$$

The current catalytic system can be envisaged as a Ni-solid solution with ceria-lanthana in which the presence of anionic vacancies can help the abstraction of H species from  $\text{CH}_4$ . The sequential decomposition of the  $\text{CH}_3$  intermediate into C, that could substitute steps 9/17 in previous models and is described as:



occurs very fast. The reversible  $\text{CO}_2$  adsorption on the support surface can happen on both  $\text{La}_2\text{O}_3$  and  $\text{Ce}_2\text{O}_3$ , generating carbonate species at the boundary of Ni particles. The subsequent reaction with adsorbed carbon generates  $\text{CO}$ , restoring the active sites.

The presence of oxygen vacancies ( $\square$ ) on the ceria-lanthana support contributes to the  $\text{CO}_2$  adsorption/dissociation step:



Diffusion of the generated lattice oxygen towards the Ni surface exerts a promoting effect in the cleaning steps (carbon oxidation to  $\text{CO}$ ) of the surface sites envisaged in the reaction sequences.

On this basis, the kinetic models proposed by Verykios's group (model 1) and Sierra-Gallego *et al.* (model 2) were applied to fit the experimental data obtained from this study over the  $\text{Ce}_{0.70}\text{La}_{0.20}\text{Ni}_{0.10}\text{O}_{2-\delta}$  catalyst. The parameters of both models were estimated using the nonlinear regression method with the ANEMONA.XLS tools, an Excel template previously developed and successfully tested with some kinetic models applied in literature for the dry reforming reaction.<sup>68</sup>

The summary of the kinetic parameters estimated from the two Langmuir-Hinshelwood rate expressions are summarized in Table 4. As evident, both models gave fitting regression coefficients ( $R^2$ ) greater than 0.90, which can be considered to be a good fitting. Thus, the models are statistically significant.

In order to evaluate the related thermodynamic relevance, the models were further screened by application of the criteria designed to evaluate the adsorption equilibrium constants obtained in a Langmuirian rate expression, defined by the following equation:<sup>69</sup>

$$10 \leq -\Delta S \leq 12.2 - 0.0014\Delta H \quad (20)$$

where  $\Delta S$  and  $\Delta H$  are the changes in entropy and enthalpy, respectively. However, the change in the entropies and enthalpies have been estimated using the Van't Hoff expression:

$$\ln K_i = \frac{-\Delta H_i}{RT} + \frac{\Delta S_i}{R} \quad (21)$$

where  $K_i$  is the adsorption constant ( $K_1$  for  $\text{CH}_4$  or  $K_3$  for  $\text{CO}_2$ ). The derived thermodynamic parameters for  $\text{CH}_4$  and  $\text{CO}_2$  and the related evaluations are synthesized in Table 5. As evident, model 2 emerges as the best kinetic model that represents the mechanism of the reaction: it satisfies the thermodynamic criterion, the  $R^2$  values (0.98 and 0.99) are considerably higher than the corresponding values derived for model 1 (0.58 and 0.89) that failed to satisfy the thermodynamic criteria.

The temperature dependence of the reaction rate parameters derived from model 2 is shown in the following



equations obtained from the Arrhenius plots (depicted in Fig. 7) of the  $K_1$ ,  $k_2$ ,  $K_3$  and  $k_4$  constants:

$$K_1 = 7.82 \times 10^{-6} \exp(8280/T) \quad (22)$$

$$k_2 = 4.80 \times 10^3 \exp(-16470/T) \quad (23)$$

$$K_3 = 7.54 \times 10^{-7} \exp(9200/T) \quad (24)$$

$$k_4 = 6.32 \times 10^2 \exp(-12110/T). \quad (25)$$

The adsorption equilibrium constants  $K_1$  and  $K_3$  increase with decreasing reaction temperature, as expected since the  $\text{CH}_4$  and  $\text{CO}_2$  adsorptions are exothermal processes. The reaction rate constants  $k_2$  and  $k_4$  follow an opposite trend. It is interesting to note that the  $k_4$  values are noticeably higher than the  $k_2$  rate constants related to the methane cracking. From this, it is possible to derive that the catalysts kinetically inhibited the carbon deposition in accordance with analogous observations reported by other authors.<sup>20,39</sup>

The absence of the carbon deposition observed in all experimental tests suggests that the catalyst stabilizes  $\text{CH}_x$  decomposition and CO disproportion that is likely the mechanism for carbon deposition during the dry reforming reaction.<sup>49</sup> The ability to activate the C–H bond cleavage requires the electron pair donation from  $\text{CH}_4$  to the unfilled d-orbital of nickel. The high d-electron density of the Ni atoms, as previously revealed by XPS studies, inhibits this process.<sup>34</sup> Similarly, the evidenced suppression of CO chemisorptions shown by this catalytic system may increase the activation barrier for CO dissociation.

The activation energies related to  $\text{CH}_4$  and  $\text{CO}_2$  were 136.9 and 100.6 kJ mol<sup>-1</sup>, respectively, which are higher than the corresponding values derived with the power law rate expression. This is reasonable considering that the Langmuir–Hinshelwood rate expression takes into account the adsorption/desorption enthalpies. Thus, the predicted values are expected to be higher than the power law expression.<sup>70</sup>

The parity plot showing the comparison between the experimental and predicted  $\text{CH}_4$  reaction rates is shown in Fig. 8. The kinetic model shows a good fit with the experimental data with a correlation coefficient of  $R^2 = 0.97$ .

## Conclusions

The kinetics of methane dry reforming over the  $\text{Ce}_{0.70}\text{La}_{0.20}\text{Ni}_{0.10}\text{O}_{2-\delta}$  catalyst has been evaluated at  $\text{CH}_4$  and  $\text{CO}_2$  partial pressures ranging between 5 to 50 kPa at 923, 973 and 1023 K. The reaction mechanism was proposed on the basis of literature and experimental observations.

The experimental data were fitted into the power law and Langmuir–Hinshelwood kinetics expression considering a dual-step with single-( $\text{Ni}^\circ$ ) and dual-active sites ( $\text{La}_2\text{O}_3$  support), respectively, for the reaction. The discrimination between the two models, statistically and thermodynamically, was evidenced as the reaction mechanism of the dry

reforming reaction over the  $\text{Ce}_{0.70}\text{La}_{0.20}\text{Ni}_{0.10}\text{O}_{2-\delta}$  catalyst. It can be described by a dual molecular adsorption of both  $\text{CH}_4$  and  $\text{CO}_2$  on metallic nickel and support ( $\text{La}_2\text{O}_3$ ), respectively, with surface reactions as the rate-determining steps. The reaction between  $\text{CO}_2$  and support generates the  $\text{La}_2\text{O}_2\text{CO}_3$  species, and is able to react with carbon at the metal–carbon interface to produce CO and clean up the metallic surface.

The high value of the kinetic constant  $k_4$  (reaction between carbonate species and carbon deposited) compared with  $k_2$  (methane cracking) suggests that the catalyst kinetically inhibits the excess of carbon deposition.

## Conflicts of interest

There are no conflicts to declare.

## References

- United Nations Framework Convention on Climate Change (UNFCCC), Adoption of the Paris Agreement, Report N. FCCC/CP/2015, <http://Unounfccc.int/resource/docs/2015/cop21/eng/l09r01.pdf>.
- J. D. Fonseca, M. Camargo, J.-M. Commengé, L. Falk and I. D. Gil, *Int. J. Hydrogen Energy*, 2019, **44**, 9486–9504.
- G. Sdanghi, G. Maranzana, A. Celzard and V. Fierro, *Renewable Sustainable Energy Rev.*, 2019, **102**, 150–170.
- A. Chapman, K. Itaoka, K. Hirose, F. T. Davidson, K. Nagasawa, A. C. Lloyd, M. E. Webber, Z. Kurban, S. Managi, T. Tamaki, M. C. Lewis, R. E. Hebner and Y. Fujii, *Int. J. Hydrogen Energy*, 2019, **44**, 6371–6382.
- K. Nagaoka, K. Takanabe and A. Ken-Ichi, *Appl. Catal., A*, 2003, **255**, 13–21.
- S. A. Chattanathan, S. Adhikari and S. Taylor, *Int. J. Hydrogen Energy*, 2012, **37**, 18031–18039.
- R. Nehring, *Philos. Trans. R. Soc., B*, 2009, **364**, 3067–3079.
- J.-M. Lavoie, *Front. Chem.*, 2014, **2**, B1.
- Y. Gao, J. Jiang, Y. Meng, F. Yan and A. Aihemaiti, *Energy Convers. Manage.*, 2018, **171**, 133–155.
- V. Nallathamb Gunaseelan, *Biomass Bioenergy*, 1997, **13**, 83–114.
- S. Gaur, D. J. Haynes and J. J. Spivey, *Appl. Catal., A*, 2011, **403**, 142–151.
- A. Fouskas, M. Kollia, A. Kambolis, C. Papadopoulou and H. Matralis, *Appl. Catal., A*, 2013, **474**, 125–134.
- J. H. Bitter, K. Sehan and J. A. Lercher, *J. Catal.*, 1991, **183**, 336–343.
- F. Menegazzo, M. Signoretto, F. Pinna, P. Canton and N. Pernicone, *Appl. Catal., A*, 2012, **439–440**, 80–87.
- D. Pakhare and J. Spivey, *Chem. Soc. Rev.*, 2014, **43**, 7813–7837.
- F. Wang, L. Xu, W. Shi, J. Zhang, K. Wu, Y. Zhao, H. Li, H. X. Li, G. Q. Xu and W. Chen, *Nano Res.*, 2017, **10**, 364–380.
- M. Usman, W. M. A. Wan Daud and H. F. Abbas, *Renewable Sustainable Energy Rev.*, 2015, **45**, 710–744.
- G. Zhang, J. Liu, Y. Xu and Y. Sun, *Int. J. Hydrogen Energy*, 2018, **43**, 15030–15054.

19 S. Arora and R. Prasad, *RSC Adv.*, 2016, **6**, 108668–108688.

20 M.-S. Fan, A. Z. Abdullah and S. Bhatia, *ChemCatChem*, 2009, **1**, 192–208.

21 W.-J. Jang, J.-O. Shim, H.-M. Kim, S.-Y. Yoo and H.-S. Roh, *Catal. Today*, 2019, **324**, 15–26.

22 I. Luisetto, S. Tuti, C. Romano, M. Boaro, E. Di Bartolomeo, J. Kopula Kesavan, S. M. Senthil Kumar and K. Selvakumar, *J. CO2 Util.*, 2019, **30**, 63–78.

23 S. Das, J. Ashok, Z. Bian, N. Dewangan, M. H. Wai, Y. Du, A. Borgna, K. Hidajat and S. Kawi, *Appl. Catal., B*, 2018, **230**, 220–236.

24 Y. Lu, D. Guo, Y. Ruan, Y. Zhao, S. Wang and X. Ma, *J. CO2 Util.*, 2018, **24**, 191–199.

25 Z. Li, M. Li, Z. Bian, Y. Kathiraser and S. Kawi, *Appl. Catal., B*, 2016, **188**, 324–341.

26 M. Steib, Y. Lou, A. Jentys and J. A. Lercher, *ChemCatChem*, 2017, **9**, 3809–3813.

27 M. Shah, S. Das, A. K. Nayak, P. Mondal and A. Bordoloi, *Appl. Catal., A*, 2018, **556**, 137–154.

28 Y. H. Hu, *Catal. Today*, 2009, **148**, 206–211.

29 V. A. Sadykov, M. N. Simonov, N. V. Mezentseva and S. N. Pavlova, *et al.*, *Open Chem.*, 2016, **14**, 363–376.

30 W.-J. Jang, D.-W. Jeong, J.-O. Shim, H.-M. Kim, W.-B. Han, J. W. Bae and H.-S. Roh, *Renewable Energy*, 2015, **79**, 91–95.

31 M. M. Makri, M. A. Vasiliades, K. C. Petallidou and A. M. Efstathiou, *Catal. Today*, 2015, **259**, 150–164.

32 L. Pino, A. Vita, F. Cipiti, M. Laganà and V. Recupero, *Appl. Catal., B*, 2011, **104**, 64–73.

33 L. Pino, A. Vita, M. Laganà and V. Recupero, *Appl. Catal., B*, 2014, **148–149**, 91–105.

34 L. Pino, C. Italiano, A. Vita, M. Laganà and V. Recupero, *Appl. Catal., B*, 2017, **218**, 779–792.

35 Y. Kathiraser, U. Oemar, E. T. Saw, Z. Li and S. Kawi, *Chem. Eng. J.*, 2015, **278**, 62–78.

36 G. Zhang, J. Liu, Y. Xu and Y. Sun, *Int. J. Hydrogen Energy*, 2018, **42**, 15030–15054.

37 V. A. Tsipouriari and X. E. Verykios, *Catal. Today*, 2001, **64**, 83–90.

38 G. Sierra Gallego, C. Batiot-Dupeyrat, J. Barrault and F. Mondrago, *Ind. Eng. Chem. Res.*, 2008, **47**, 9272–9278.

39 Z. Bao, Y. Lu and F. Yu, *AIChE J.*, 2017, **63**, 2019–2029.

40 D. E. Mears, *Ind. Eng. Chem. Process Des. Dev.*, 1971, **10**, 541–547.

41 M. E. Davis and R. J. Davis, *Fundamental of chemical reaction engineering*, McGraw-Hill, New York, 2003, pp. 184–239.

42 P. B. Weisz and C. D. Prater, *Adv. Catal.*, 1954, **6**, 143–196.

43 S. Wang and G. Q. Lu, *Ind. Eng. Chem. Res.*, 1999, **38**, 2615–2625.

44 A. A. Lemonidou and I. A. Vasalos, *Appl. Catal., A*, 2002, **228**, 227–235.

45 A. Nandini, K. K. Pant and S. C. Dhingra, *Appl. Catal., A*, 2006, **308**, 119–127.

46 J. Zhang, H. Wang and A. K. Dalai, *Ind. Eng. Chem. Res.*, 2009, **48**, 677–684.

47 J. Dacquin, D. Sellam, C. Batiot-Dupeyrat, A. Tougerti, D. Duprez and S. Royer, *ChemSusChem*, 2014, **7**, 631–637.

48 S. Das, S. Thakur, A. Bag, M. S. Gupta, P. Mondal and A. Bordoloi, *J. Catal.*, 2015, **330**, 46–60.

49 M. C. J. Bradford and M. A. Vannice, *Appl. Catal., A*, 1996, **142**, 97–122.

50 M. C. J. Bradford and M. A. Vannice, *Catal. Rev.: Sci. Eng.*, 1991, **41**, 1–42.

51 F. A. J. Al-Doghachi, U. Rashid, Z. Zainal, M. I. Saiman and Y. H. T. Yap, *RSC Adv.*, 2015, **5**, 81739–81752.

52 X. E. Verykios, *Int. J. Hydrogen Energy*, 2003, **28**, 1045–1063.

53 J. F. Munera, S. Irusta, L. M. Cornaglia, E. A. Lombardo, D. V. Cesar and M. Schmal, *J. Catal.*, 2007, **245**, 25–34.

54 J. F. Munera, L. Cornaglia, D. V. Cesar, M. Schmal and E. A. Lombardo, *Ind. Eng. Chem. Res.*, 2007, **46**, 7543–7549.

55 O. U. Osazuwa, H. D. Setiabudi, S. Abdullah and C. K. Cheng, *Int. J. Hydrogen Energy*, 2017, **42**, 9707–9721.

56 A. M. Brown, *Comput. Methods Programs Biomed.*, 2001, **65**, 191–200.

57 M. D. A. Hossain, H. H. Ngo and W. Guo, *J. Water Sustainability*, 2013, **3**, 223–237.

58 V. C. H. Kroll, G. J. Tjatjopoulos and C. Mirodatos, *Natural Gas Conversion V. (Stud. Surf. Sci. Catal.)*, 1998, vol. 119, pp. 753–758.

59 A. Takano, T. Tagawa and S. Goto, *J. Chem. Eng. Jpn.*, 1994, **27**, 727–731.

60 B. Ayodele, M. R. Khan, S. S. Lam and C. K. Cheng, *Int. J. Hydrogen Energy*, 2016, **41**, 4603–4615.

61 X. Yan, T. Hu, P. Liu, S. Li, B. Zhao, Q. Zhang, W. Jiao, S. Chen, P. Wang, J. Lu, L. Fan, X. Deng and Y.-X. Pan, *Appl. Catal., B*, 2019, **246**, 221–231.

62 R. K. Singha, A. Yadav, A. Agrawal, A. Shukla, S. Adak, T. Sasaki and R. Bal, *Appl. Catal., B*, 2016, **191**, 165–178.

63 U. Oemar, Y. Kathiraser, L. Mo, X. K. Ho and S. Kawi, *Catal. Sci. Technol.*, 2016, **6**, 1173–1186.

64 L. M. Aparicio, *J. Catal.*, 1997, **165**, 262–274.

65 Z. Zhang, X. E. Verykios, S. M. MacDonald and S. Affrossman, *J. Phys. Chem.*, 1996, **100**, 744–754.

66 V. A. Tsipouriari and X. E. Verykios, *J. Catal.*, 1999, **187**, 85–94.

67 A. Slagtern, Y. Schuurman, C. Leclercq, X. Verykios and C. Mirodatos, *J. Catal.*, 1997, **172**, 118–126.

68 L. Pino, V. Recupero and A. Hernández, *ChemEngineering*, 2018, **2**, 57.

69 M. A. Vannice, *Kinetics of catalytic reactions*, Springer, New York, 2005, pp. 106–137.

70 I. Chorkendorff and J. M. Niemantsverdriet, *Concept of modern Catalysis and Kinetics*, Wiley-VCH Verlag GmbH & Co. KGaA, 2005, pp. 23–78.

